

Morphological image analysis of quantum motion in billiards

J. S. Kole, K. Michielsen, and H. De Raedt

Institute for Theoretical Physics and Materials Science Centre, University of Groningen, Nijenborgh 4, NL-9747 AG Groningen, The Netherlands

(Received 7 July 2000; published 18 December 2000)

Morphological image analysis is applied to the time evolution of the probability distribution of a quantum particle moving in two- and three-dimensional billiards. It is shown that the time-averaged Euler characteristic of the probability distribution provides a well defined quantity to distinguish between classically integrable and nonintegrable billiards. In three dimensions the time-averaged mean breadth of the probability distribution may also be used for this purpose.

DOI: 10.1103/PhysRevE.63.016201

PACS number(s): 05.45.-a, 03.65.Sq, 02.70.-c

I. INTRODUCTION

In the theory of quantum chaos, the connection between the chaotic behavior of classical systems and specific properties of their quantum mechanical counterparts has received much attention. The most studied issues in this context are the statistical properties of nuclear and atomic spectra [1] and of two- (recently three-) dimensional billiards [2–5]. In the mid, 1980s, a conjecture (which became known as the Bohigas-Giannoni-Schmidt (BGS) conjecture [6]) was made that the quantal energy level spacing of (ergodic) systems whose classical equivalent exhibits a chaotic behavior obeys Wigner Gaussian orthogonal ensemble statistics, known from random matrix theory, whereas for classically integrable systems the Poisson distribution applies. Exceptions to this conjecture are known [7,8], but it is generally believed that these form a set of measure 0.

Another way to make a connection between the chaotic behavior of classical systems and specific properties of their quantum mechanical counterparts is to look at the eigenstates of billiards. Eigenstates of a stadium may exhibit a structure that corresponds to classical orbits [9–11]. These structures, called scars, have been directly related to unstable periodic orbits [12–14]. Visual inspection of movies that show the time evolution of the probability distribution of a quantum particle moving in two- and three-dimensional (2D and 3D) billiards of different shapes strongly suggests that these sequences of images may contain enough information to distinguish between classically integrable and chaotic systems [15].

To our knowledge the morphology of patterns of time (in)dependent probability distributions has not been studied. In this paper we propose a method, based on concepts from integral geometry, to perform a morphological image analysis (MIA) of the probability distribution. We use MIA to characterize the solutions of the time-dependent Schrödinger equation for various 2D and 3D billiards. We demonstrate that, indeed, one can define geometrical and topological descriptors that are useful to distinguish between classically integrable and chaotic billiards. Our motivation to analyze time-dependent instead of stationary probability distributions is that the former usually provide information about many eigenstates simultaneously. By following the system over a sufficiently long period of time, one collects information on

all those eigenstates that have non-negligible overlap with the initial state. This “parallelism,” absent in the stationary-state approach [16], reduces the computational work.

MIA amounts to a characterization of the geometry and topology of any pattern or series of patterns by means of the so-called Minkowski functionals, known from integral geometry [17–19]. These functionals are related to familiar quantities: In two (three) dimensions, they correspond to the covered area, perimeter, and connectivity (volume, surface area, integral mean curvature, and connectivity) of the pattern. In integral geometry the calculation of the Minkowski functionals is relatively straightforward, and requires little computational effort. MIA has proven to be a powerful tool in different fields where the description of patterns is important: statistical physics, to describe the morphology of porous media and complex fluids; cosmology, to analyze the large scale distribution of matter in the universe; chemistry, to describe the morphology of patterns in reaction diffusion systems [20]; seismology, to describe the spatial complexity of regional seismicity realizations [21]; and polymer science, to identify and quantify the morphology of mesoscale structures in block copolymers [22,23]. Furthermore, in the semiclassical limit the sum of exponentials of eigenfrequencies of a billiard-shaped drum can be written in terms of the Minkowski functionals of the billiard [24], and the Weyl hypothesis states that the number of energy levels up to an energy E can be written in a similar manner (see, e.g., Ref. [25]).

In Sec. II we briefly review the theory of Minkowski functionals, and explain the technique of MIA in more detail. We then apply MIA to the motion of a quantum particle in various two- and three-dimensional billiards, and show that an appropriate quantity can be defined to distinguish classically integrable and chaotic billiards. Finally, we study the transition to chaos for a system whose degree of chaos is parametrized.

II. MORPHOLOGICAL IMAGE ANALYSIS

At the heart of MIA lies the computation of Minkowski functionals of an arbitrary (thresholded) image. Therefore, in this section we will give some mathematical background on Minkowski functionals (closely following Ref. [20]), and sketch the outline of an algorithm to compute these functionals.

We first define the Minkowski functionals for compact convex sets. The parallel set K_r of a compact convex set K at a distance r is the union of all closed balls of radius r , the centers of which are points in K . The well-known Euclidean measures of K_r , such as the area and volume, can be written as polynomials in r . For example, the parallel volume of a square S and a cube C with edge lengths a are given by

$$V_r(S) = a^2 + 4ar + \pi r^2, \quad (1)$$

$$V_r(C) = a^3 + 6a^2r + 3\pi ar^2 + 4\pi r^3/3. \quad (2)$$

In general, the volume $v^{(d)}$ in d dimensions of the parallel set K_r at distance r of K is given by the Steiner formula [17]

$$v^{(d)}(K_r) = \sum_{v=0}^d \binom{d}{v} W_v^{(d)}(K) r^v, \quad (3)$$

where $W_v^{(d)}(K)$ are the Minkowski functionals. For the first three dimensions it can be shown that [17]

$$d=1: \quad W_0^{(1)}(K) = l(K), \quad W_1^{(1)} = 2\chi(K), \quad (4)$$

$$d=2: \quad W_0^{(2)}(K) = A(K), \quad W_1^{(2)} = \frac{1}{2}U(K),$$

$$W_2^{(2)} = \pi\chi(K), \quad (5)$$

$$d=3: \quad W_0^{(3)}(K) = V(K), \quad W_1^{(3)} = \frac{1}{3}S(K),$$

$$W_2^{(3)}(K) = \frac{2}{3}\pi B(K), \quad W_3^{(3)}(K) = \frac{4\pi}{3}\chi(K), \quad (6)$$

where $l(K)$, $A(K)$, $U(K)$, $V(K)$, $S(K)$, $B(K)$, and $\chi(K)$ denote the length, area, perimeter, volume, surface area, mean breadth, and Euler characteristic or connectivity number of the convex set K , respectively. The mean breadth B is closely related to the mean curvature $H = (R_1 + R_2)/2R_1R_2$, where R_1 and R_2 are the principal radii of curvature [26]. The Euler characteristic χ is related to the Gaussian curvature $G = 1/R_1R_2$, and is equal to unity for a convex body [26]. The mean curvature and the Gaussian curvature are two useful measures of the curvature of a surface [26]. If the local surface geometry has an elliptic, Euclidean, or hyperbolic shape, respectively, then the Gaussian curvature is respectively positive, zero, or negative [26].

Up to now, we have limited the discussion to convex sets. In order to deal with the more general sets one encounters in characterizing images, we consider the convex ring \mathcal{R} , which is the class of all subsets A which can be expressed as finite unions of compact convex sets K_i :

$$A = \bigcup_{i=1}^l K_i. \quad (7)$$

The Euler characteristic χ is defined as an additive functional on \mathcal{R} , so that, for $A \in \mathcal{R}$,

$$\chi(A) = \chi\left(\bigcup_{i=1}^l K_i\right)$$

$$= \sum_i \chi(K_i) - \sum_{i < j} \chi(K_i \cap K_j)$$

$$+ \dots + (-1)^{l+1} \chi(K_1 \cap \dots \cap K_l), \quad (8)$$

and where, for compact convex sets K ,

$$\chi(K) = \begin{cases} 1 & \text{if } K \neq \emptyset \\ 0 & \text{if } K = \emptyset \end{cases}. \quad (9)$$

The Euler characteristic describes A in a pure topological way, i.e., without reference to any kind of metric. It can be shown that this definition of χ permits all Minkowski functionals on \mathcal{R} to be written in terms of χ and the kinematical density [17]. The functional χ as defined in integral geometry is the same as the Euler characteristic defined in algebraic topology [17]: For $d=2$, χ equals the number of connected components minus the number of holes, and in three dimensions χ is given by the number of connected components minus the number of tunnels plus the number of cavities. For example, for a solid cube $\chi=1$, for a hollow cube $\chi=2$, and for a cube pierced by a tunnel $\chi=0$. For multiply connected structures the Euler characteristic is negative. For complex structures it is often difficult to identify the number of connected components, tunnels and cavities. However, MIA directly yields χ , as will be explained below.

In order to calculate the morphological properties of a particular image, we first convert the image to a black-and-white picture using a threshold. Pixels (voxels) with an intensity below the threshold are considered to be part of the background and the others are building up the objects in the 2D (3D) picture. According to integral geometry, the morphological properties of the various objects building up the black-and-white picture can be completely described in terms of Minkowski functionals [17]. In order to calculate the Minkowski functionals in an efficient way we consider each pixel (voxel) as the union of the disjoint collection of its interior, faces (for the 3D case only), open edges and vertices. The values of A , U , V , S , B , and χ for these single open structures can easily be calculated [27]. By making use of the property of additivity of the Minkowski functionals and the fact that there is no overlap between open bodies on a lattice, we compute the Minkowski functionals of the whole image by starting from a complete white image, calculating the change in the number of interiors, faces (for the 3D case only), open edges and vertices when one pixel (voxel) is added to the 2D (3D) image, and this until all pixels (voxels) building up the picture are added. The Minkowski functionals can then be computed from

$$d=2: \quad A = n_s, \quad U = -4n_s + 2n_e, \quad \chi = n_s - n_e + n_v, \quad (10)$$

$$d=3: \quad V = n_c \quad S = -6n_c + 2n_f, \quad 2B = 3n_c - 2n_f + n_e,$$

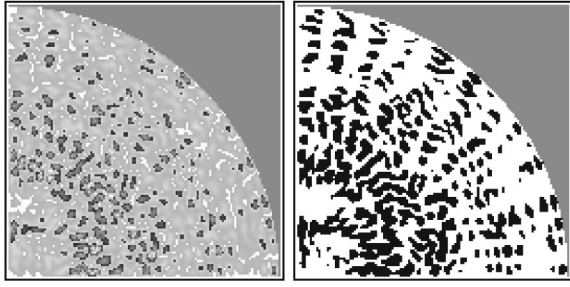


FIG. 1. Snapshot of the probability distribution at time $t=319$ (in dimensionless units; see the text) in the case of a billiard in the form of a quarter circle (left) and its thresholded counterpart using a threshold $\theta=10\%$ (right). The background is colored white, the objects black, and the forbidden region for the quantum particle gray.

$$\chi = -n_c + n_f - n_e + n_v, \quad (11)$$

where n_s (n_c) denote the number of squares (cubes) in two (three) dimensions, n_f counts the number of faces (in three dimensions only), n_e and n_v denote the number of edges and vertices, respectively. From Eqs. (10) and (11) it follows directly that the Minkowski functionals contain information about local four- (eight-) point correlation functions in two (three) dimensions. A more detailed description of the algorithm and an example of computer code to compute the Minkowski functionals is given in Ref. [27].

III. METHOD

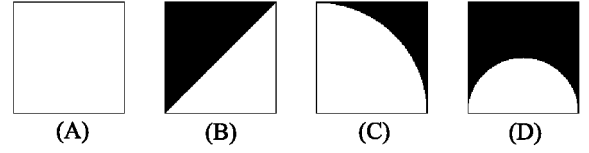
The application of MIA to the time evolution of the probability distribution of a quantum particle moving in a billiard is straightforward. We solve the time-dependent Schrödinger equation for a particle moving in a billiard by a stable and accurate numerical method [28]. For practical purposes the results obtained are exact. A time series of snapshots displaying the probability distribution can easily be extracted from these data. A collection of digital videos can be found in Ref. [15]. Each pattern of the time series is converted into a black-and-white picture by applying a threshold. The result of applying a threshold of 10% to a representative image of the probability distribution is shown in Fig. 1.

For each black-and-white image in the time series we compute the Minkowski functionals using the algorithm described above, and analyze the behavior of the Minkowski functionals as a function of control parameters such as the threshold, the initial conditions of the wave packet, and the shape of the billiard. We use Gaussian wave packets as initial states, and study a variety of classically integrable and nonintegrable billiards (see Figs. 2–4).

In our numerical work we express lengths in units of a fixed wavelength λ , and rescale energy (and time, setting $\hbar = 1$) such that a wave packet with average momentum $2\pi/\lambda$ has an average kinetic energy of 1 [28].

As will become clear from the examples given below, to distinguish between classically integrable and chaotic systems it is expedient to define the time-averaged Minkowski functionals

Classically Integrable Billiards



Classically Non-integrable Billiards

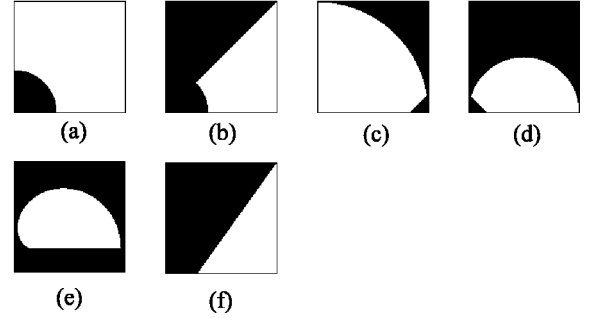


FIG. 2. The shapes of the various two-dimensional billiards studied: square (A), equilateral triangle (B), quarter circle (C), semicircle (D), perturbed square (a), perturbed equilateral triangle (b), perturbed quarter circle (c), perturbed semicircle (d), semicircle (e), and triangle with sides which ratio is irrational (f). The billiards are colored white, and the forbidden regions for the quantum particle are colored black. In most calculations the linear size of the square was taken to be 13λ .

$$X(T, \theta) = \frac{1}{\bar{A}T} \int_0^T \chi(t, \theta) dt, \quad \mathbf{B}(T, \theta) = \frac{1}{\bar{A}T} \int_0^T \mathbf{B}(t, \theta) dt, \quad (12)$$

and the quantities

$$X(\theta) = \lim_{T \rightarrow \infty} X(T, \theta), \quad \mathbf{B}(\theta) = \lim_{T \rightarrow \infty} \mathbf{B}(T, \theta), \quad (13)$$

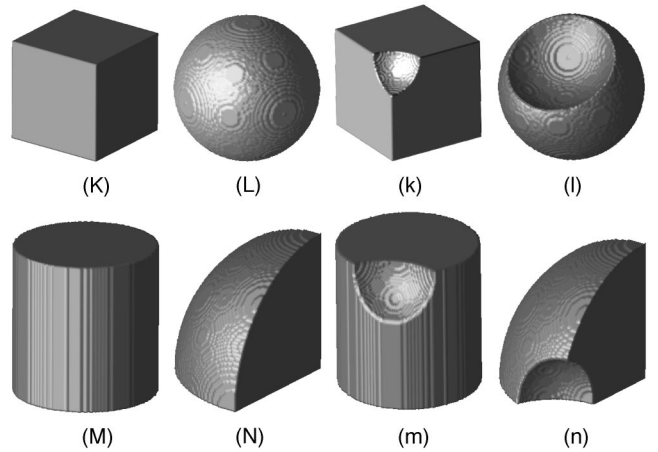


FIG. 3. The shapes of the various three-dimensional billiards studied: cube (K), sphere (L), cylinder (M), one eighth of a sphere (N), perturbed cube (k), perturbed sphere (l), perturbed cylinder (m), and perturbed one eighth of a sphere (n). In most calculations the sides of the bounding cube (not shown) were taken to be 9.5λ .

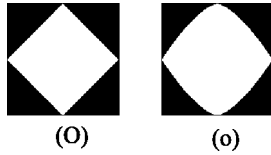


FIG. 4. Two instances of the lemon-shaped billiard, with boundaries in the x - y plane defined by $y(x) = \pm(1 - |x|^\delta)$, $x \in [-1, 1]$. $\delta = 1$ (O), and $\delta = 1.5$ (o). The billiards are colored white, and the forbidden regions for the quantum particle are colored black. In most calculations the linear size of the square was taken to be 13λ .

$$\mu(\chi) = \max_{\theta} X(\theta), \quad \mu(B) = \max_{\theta} \mathbf{B}(\theta), \quad (14)$$

where $\tilde{A} = \lambda^2/A$ ($\tilde{A} = \lambda^3/V$) in two (three) dimensions.

IV. 2D RESULTS

In Fig. 5 we present results that illustrate the typical behavior of the Minkowski functionals as a function of time, keeping the threshold fixed. The top panel of Fig. 5 shows the perimeter $U(t, \theta)$ as a function of time t for billiards (A) and (a) using a threshold $\theta = 5\%$. Billiard (A) (solid line) shows a behavior which is manifestly different from that of billiard (a) (dashed line): For times $t > 100$ the solid line displays large fluctuations, in contrast to the dashed line. Other pairs of billiards (B) and (b), etc. show very similar, characteristic fluctuations in the perimeter as a function of time (results not shown). Essentially the same behavior is

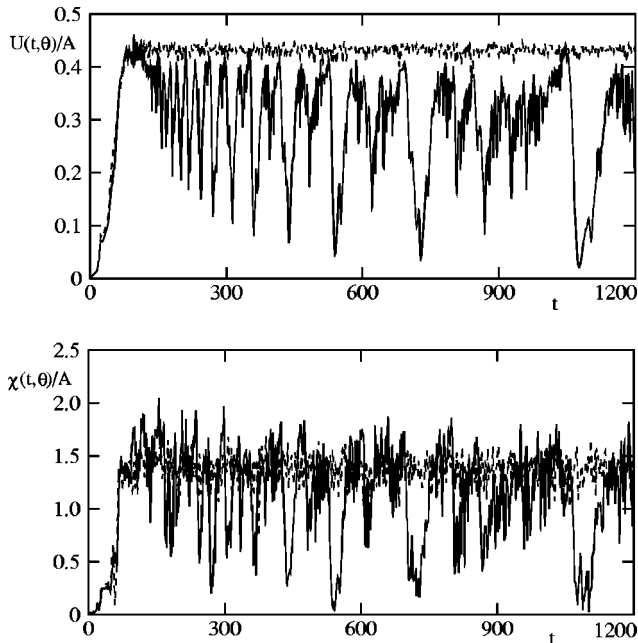


FIG. 5. Top: perimeter $U(t, \theta)$ (in pixels), normalized to the area A of the billiard (in pixels), as a function of time t using a threshold $\theta = 5\%$. Solid line: billiard (A). Dashed line: Billiard (a). Bottom: Euler characteristic $\chi(t, \theta)$, normalized to the area of the billiard (in pixels), as a function of time t using a threshold $\theta = 15\%$. Solid line: billiard (B). Dashed line: billiard (b). The time is measured in dimensionless units (see the text).

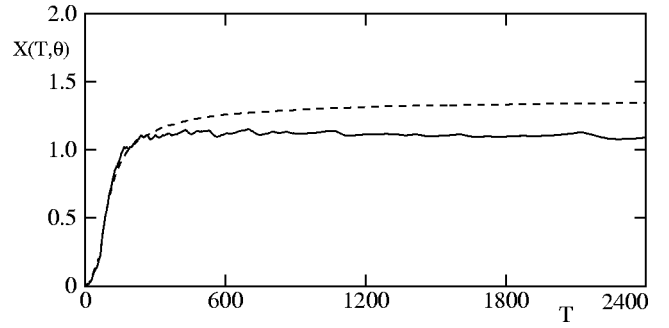


FIG. 6. $X(T, \theta)$ as a function of time T , using a threshold $\theta = 15\%$. $X(T, \theta)$ and T are measured in dimensionless units (see text). Solid line: billiard (B). Dashed line: billiard (b).

found for the Euler characteristic $\chi(\theta, t)$. An example is given in the bottom panel of Fig. 5 for the case of billiards (B) and (b) and $\theta = 15\%$. Hence, in conclusion, for integrable billiards $U(t, \theta)$ and $\chi(t, \theta)$ show large fluctuations, while for nonintegrable billiards these large fluctuations do not occur.

Since the Euler characteristic $\chi(t, \theta)$ is a global measure of the curvatures of the objects in the black-and-white image, and provides direct quantitative information about the topology of the probability distribution (see Ref. [18], pp. 34, 112, and 113) we will study the behavior of χ as a function of t and θ in more detail. For each choice of the threshold θ , the cumulative time average of the Euler characteristic $X(T, \theta)$ approaches a constant value which we denote by $X(\theta)$. A representative example of the behavior of $X(T, \theta)$ is shown in Fig. 6.

In Fig. 7 we plot the results for $X(\theta)$, for each of the billiards of Fig. 2. As θ approaches zero, the thresholded black-and-white picture becomes completely filled with black pixels; hence $\lim_{\theta \rightarrow 0} X(\theta) = \lambda^2/A$ for any image. Obviously, for $\theta \rightarrow 0$, $X(\theta)$ does not contain any useful information, and for reasons of clarity we therefore omit data for $\theta < 1$ in Fig. 7.

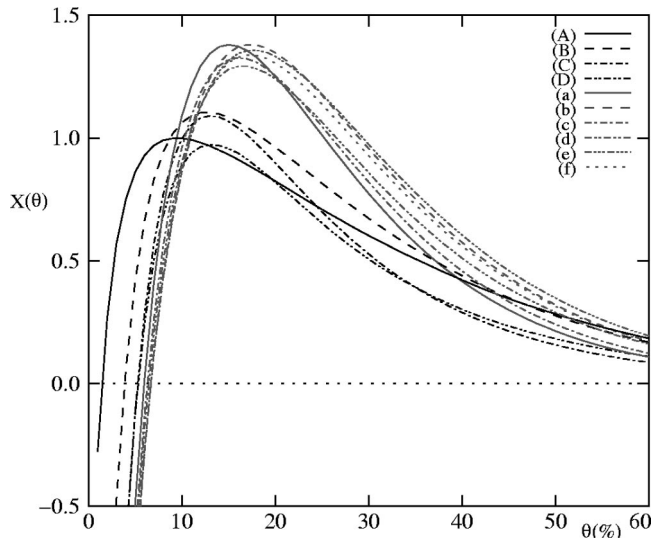


FIG. 7. $X(\theta)$ as function of the threshold θ (in percent), for all billiards shown in Fig. 2.

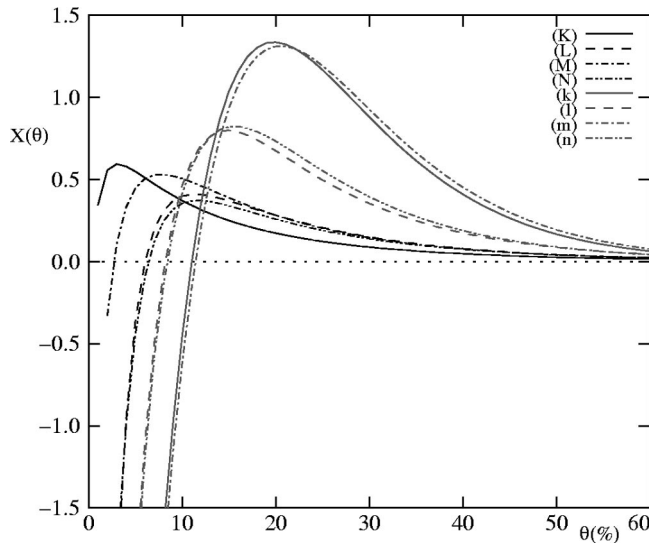


FIG. 8. $X(\theta)$ as a function of the threshold θ (in percent), for all billiards shown in Fig. 3.

From Fig. 7 it is clear that the $X(\theta)$ curves form two clusters, depending on whether the system is classically integrable or not. In fact, $\mu(\chi)$, can be used to classify billiards according to their classical (non)integrability, as shown in Table I. The maxima for the classically integrable systems all lie in the range $[0.97, 1.10]$, whereas the maxima for the classically nonintegrable systems lie in the range $[1.29, 1.38]$. Further analysis indicates that the maximum of $X(\theta)$ changes linearly with the energy of the wave packet (results not shown). This scaling behavior could be trivially incorporated into the definition of $X(\theta)$. Calculations (results not shown) for systems up to $19\lambda \times 19\lambda$ suggest that the system size dependence of $X(\theta)$ is very weak. Therefore, we conclude that the scaling properties of $\mu(\chi)$ can be employed to test for the (non)integrability of billiards. In contrast to what Fig. 5 (top) might suggest, the cumulative time average and

TABLE I. $\mu(\chi)$ and the corresponding θ for all billiards shown in Fig. 2.

Billiard	θ	$\mu(\chi)$
(A)	10	1.00
(B)	13	1.10
(C)	13	1.09
(D)	13	0.97
(a)	15	1.38
(b)	17	1.38
(c)	16	1.33
(d)	17	1.29
(e)	18	1.36
(f)	17	1.34

TABLE II. $\mu(\chi)$ and the corresponding θ for all billiards shown in Fig. 3.

Billiard	θ	$\mu(\chi)$
(K)	3	0.59
(L)	11	0.41
(M)	8	0.53
(N)	12	0.37
(k)	20	1.34
(l)	15	0.80
(m)	21	1.31
(n)	16	0.82

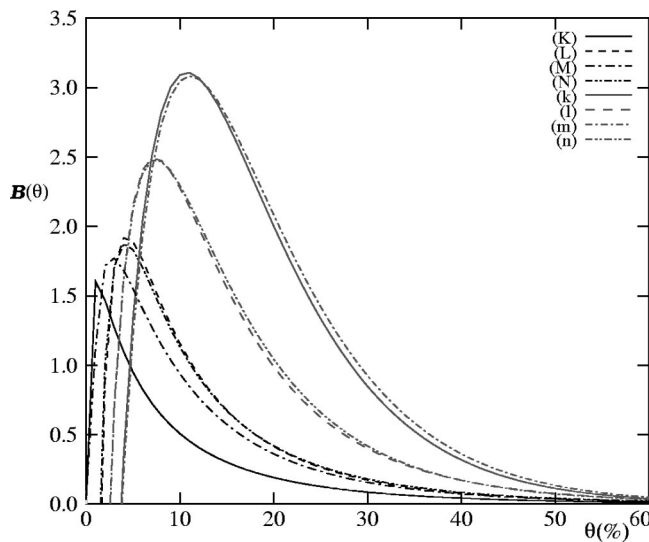


FIG. 9. $B(\theta)$ as a function of the threshold θ (in percent), for all billiards shown in Fig. 3.

TABLE III. $\mu(B)$ and the corresponding θ for all billiards shown in Fig. 3.

Billiard	θ	$\mu(B)$
(K)	1	1.60
(L)	4	1.92
(M)	3	1.77
(N)	4	1.87
(k)	11	3.10
(l)	7	2.49
(m)	11	3.08
(n)	7	2.47

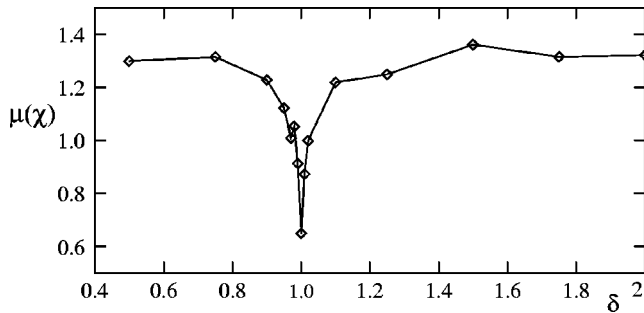


FIG. 10. $\mu(\chi)$ as function of the shape parameter δ for the lemon-shaped billiard. For $\delta=1$, the billiard is integrable.

its infinite time limit of the perimeter U (and also the area A) do not have the same properties as $X(T, \theta)$ and $X(\theta)$ (results not shown). Hence in two dimensions only $\mu(\chi)$ can be used to test for the (non)integrability of billiards.

V. 3D RESULTS

For three-dimensional billiards not much research has been done on the issue of characterizing classical chaos on basis of some quantum mechanical property. Very recently, results of numerical work on the stability of classical trajectories [29], and on 3D Sinai billiards [5], was reported, but much of the field is unexplored.

In order to look for a quantum signature of chaos in 3D billiards (see Fig. 3), we apply an analogous approach to the one described above for the 2D billiards. In three dimensions both the mean breadth B and the Euler characteristic χ may be used to distinguish integrable and nonintegrable billiards. From Figs. 8 and 9 it is clear that the $X(\theta)$ and $\mathbf{B}(\theta)$ curves form two groups depending on whether the billiards are integrable or not. As was the case for the 2D billiards, we can again use the maximum values of these curves to classify the billiards according to their classical (non) integrability, as shown in Tables II and III. For classically integrable systems $\mu(B)$ lies in the range [1.60,1.9,2], whereas for nonintegrable systems $\mu(B)$ lies in the range [2.47,3.10], a significant difference. For the Euler characteristic, these ranges are [0.37–0.59] for integrable systems and [0.80,1.34] for non-integrable ones. Here the separation is less in magnitude but still present.

VI. TRANSITION TO CHAOS

An interesting case to confirm that $\mu(\chi)$ can be used to detect a transition from integrable to chaotic behavior is the lemon-shaped billiard [4]. Two instances of the lemon-shaped billiard are shown in Fig. 4. The boundaries in the x - y plane are defined by $y(x) = \pm(1 - |x|^\delta)$, $x \in [-1, 1]$. The integrability of the lemon-shaped billiard depends on the shape parameter δ : For $\delta=1$ and $\delta=\infty$ the billiard is integrable; otherwise it is not. If δ slightly deviates from 1, the billiard is classically partially chaotic (periodic orbits and chaotic trajectories coexist). Figure 10 shows $\mu(\chi)$ for the lemon-shaped billiard, for a shape parameter δ varying between 0.5 and 2.0.

The sharp peak centered around $\delta=1$ shows that $\mu(\chi)$ is

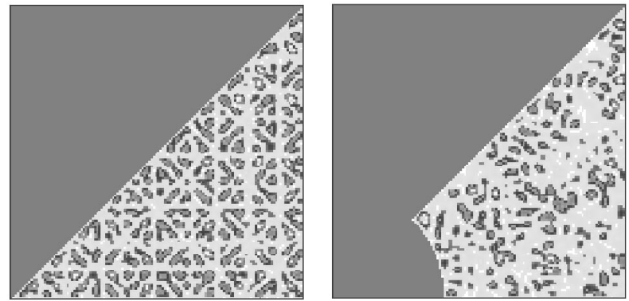


FIG. 11. Snapshot at time $t=8$ of the probability distribution of a quantum particle moving in billiards (B) (left) and (b) (right).

very sensitive to the presence of classically unstable trajectories. If there are any unstable trajectories in the classical system, the value of $\mu(\chi)$ for the quantum mechanical equivalent can be classified as chaotic. Thus the curve in Fig. 10 clearly shows the transition from chaotic to integrable behavior, and vice versa.

VII. CONCLUSION

We have described a method, based on concepts of integral geometry, to analyze the time evolution of the probability distribution of a quantum particle moving in two- and three-dimensional billiards. We have demonstrated that the time-averaged Euler characteristic can be used to classify billiards as integrable or not. A qualitative explanation for this may be the following: The eigenstates of a billiard contain information about the chaotic behavior. Since the time-dependent probability distribution of a quantum particle moving in a billiard contains information about many eigenstates simultaneously, it also contains information about the (non)chaotic behavior of the billiard. The time evolution of the probability distribution of a quantum particle moving in classically integrable and nonintegrable billiards looks very different. A clear example is given in Fig. 11 for the case of billiards (B) and (b). While the time-dependent probability distribution for billiard (B) is rather symmetric and periodic, the one for billiard (b) looks rather “chaotic.” This difference in behavior is reflected in the time-averaged Euler characteristic, which characterizes the topology of the patterns.

For three-dimensional billiards, the time-averaged mean breadth (or integral mean curvature) of the probability distribution can also be employed for this purpose. For lemon-shaped billiards we have shown that the transition from integrable to chaotic behavior can be determined from the dependence of the time-averaged Euler characteristic on the parameter that controls the shape of the billiard. We believe it may also be of interest to apply the method described in this paper to the time-independent solutions.

ACKNOWLEDGMENTS

We would like to thank the Dutch “Stichting Nationale Computer Faciliteiten” (NCF) for their support, and A. Lande for his critical reading of the manuscript.

- [1] S. Blumberg and G. E. Porter, Phys. Rev. **110**, 786 (1958).
- [2] M. V. Berry and M. Tabor, Proc. R. Soc. London, Ser. A **356**, 375 (1977).
- [3] S. W. McDonald and A. N. Kaufman, Phys. Rev. Lett. **42**, 1189 (1979).
- [4] V. Lopac, I. Mrkonjić, and D. Radić, Phys. Rev. E **59**, 303 (1999).
- [5] H. Primack and U. Smilansky, Phys. Rep. **327**, 1 (2000).
- [6] O. Bohigas, M. Giannoni, and C. Schmidt, Phys. Rev. Lett. **52**, 1 (1984).
- [7] J. Zakrzewski, K. Dupret, and D. Delande, Phys. Rev. Lett. **74**, 522 (1995).
- [8] P. Crehan, J. Phys. A **28**, 6389 (1995).
- [9] S. W. McDonald (unpublished).
- [10] R. D. Taylor and P. Brumer, Faraday Discuss. Chem. Soc. **75**, 170 (1983).
- [11] E. J. Heller, Phys. Rev. Lett. **53**, 1515 (1984).
- [12] E. B. Bogomolny, Physica D **31**, 169 (1988).
- [13] M. V. Berry, Proc. R. Soc. London, Ser. A **423**, 219 (1989).
- [14] M. Feingold, R. G. Littlejohn, S. B. Solina, and J. S. Pehling, Phys. Lett. A **146**, 199 (1990).
- [15] <http://rugth30.phys.rug.nl/compphys/chaos.htm>
- [16] B. Li, M. Robnik, and B. Hu, Phys. Rev. E **57**, 4095 (1998).
- [17] H. Hadwiger, *Vorlesungen über Inhalt, Oberfläche und Isoperimetrie* (Springer-Verlag, Berlin, 1957).
- [18] L. A. Santaló, *Integral Geometry and Geometric Probability* (Addison-Wesley, Reading, MA, 1976).
- [19] D. Stoyan, W. S. Kendall, and J. Mecke, *Stochastic Geometry and its Applications* (Akademie Verlag, Berlin, 1989).
- [20] K. R. Mecke, Int. J. Mod. Phys. B **12**, 861 (1998).
- [21] N. G. Makarenko, L. M. Karimova, A. G. Terekhov, and A. V. Kardashev, Phys. Solid Earth **36**, 305 (2000).
- [22] K. Michielsen, H. De Raedt, and T. Kawakatsu, in *Computer Simulation Studies in Condensed Matter Physics XIII*, edited by D. P. Landau, K. K. Mon, and H. D. Schütler (Springer-Verlag, Berlin, in press).
- [23] K. Michielsen, H. De Raedt, and J. G. E. M. Fraaije, Prog. Theor. Phys. Suppl. **138**, 543 (2000).
- [24] M. Kac, Am. Math. Monthly **73**, 1 (1966).
- [25] H. P. Baltes and E. R. Hilf, *Spectra of Finite Systems* (Bibliographisches Institut, Mannheim, 1976).
- [26] S. Hyde, S. Andersson, K. Larsson, Z. Blum, T. Landh, S. Lidin, and B. W. Ninham, *The Language of Shape; The Role of Curvature in Condensed Matter: Physics, Chemistry and Biology* (Elsevier, Amsterdam, 1997).
- [27] K. Michielsen and H. De Raedt, Comput. Phys. Commun. **132**, 94 (2000).
- [28] H. De Raedt and K. Michielsen, Comput. Phys. **8**, 600 (1994).
- [29] T. Papenbrock, Phys. Rev. E **61**, 4626 (2000).